Zuschriften

Nanostructured Zinc Oxide Nanorods with Copper Nanoparticles as a Microreformation Catalyst**

Yan-Gu Lin, Yu-Kuei Hsu, San-Yuan Chen, Yu-Kai Lin, Li-Chyong Chen, and Kuei-Hsien Chen*

The use of hydrogen for energy generation has attracted significant attention in recent years as a clean, sustainable, and transportable alternative fuel, and this interest has consequently sparked a rapid global development of hydrogen fuel cells for electric power generation.[1] Catalytic reformation of hydrocarbons, with careful attention to avoid storage and safety issues,[2,3] is currently the predominant process for hydrogen generation. One of the leading and most promising techniques for hydrogen generation is catalytic reformation of methanol.[4,5] Cu/ZnO-based catalysts are, therefore, of great importance for industrial scale catalytic production of reformate hydrogen.[6] Owing to their wide commercial relevance, Cu/ZnO-based catalysts, prepared by several preparation routes, are being extensively investigated, and substantial improvements in their efficiency of catalytic activity brought about by addition of suitable promoter/support, combination with effective component, and implementation of new preparation techniques, have been reported.[4,5,7–12] Unfortunately, use of Cu/ZnO-based heterostructures as reforming catalysts is still lacking to date. This inspired us to design a core–shell nanostructured catalyst consisting of a ZnO nanorod (NR) core and an outer shell of copper nanoparticles (NPs), that is, NR@NPs, for achieving high efficiency of catalytic conversion.

The idea of using microreformers is also highly attractive for several applications, such as on-board hydrogen sources for small vehicles and portable fuel cells.[13,14] However, two key issues have hindered the realization of microreformers for catalysis, namely, poor adhesion between the catalyst layer and the microchannels and poor utilization of catalyst layer deposited in the form of thick film.[15] Notwithstanding, several approaches investigated to overcome these issues,

catalyst immobilization, and its efficient utilization inside the microchannel remains a challenge.[16,17] Most of these approaches involve a two-step process, wherein active catalysts are prepared in the first step, followed by its immobilization on the surface of the microchannels in the second step. Herein, we report a simple and reliable method for integrating in-situ synthesis of catalyst and its immobilization for microreformer applications.

The ZnO NR arrays were first grown on a microchannel reactor using a simple template-free aqueous approach. A simple mixture of copper salts, aqueous media, and ZnO NR arrays at low temperature subsequently resulted in spontaneous formation of cable-like nanostructures. As the ZnO NR@Cu NP nanocomposites were synthesized in-situ directly on the microreactor, the arrayed ZnO@Cu nanocomposites were strongly anchored onto the microchannel. The strong mechanical anchorage of nanostructured catalysts on the surface of microchannel was shown by the observation that no material loss occurred after sonication in the water for several hours. The interaction between Cu NPs and ZnO NRs was studied by several analytical techniques, including electron microscopy (EM), X-ray diffraction (XRD), X-ray photoelectron spectroscopy (XPS), X-ray absorption spectroscopy (XAS), and temperature-programmed reduction (TPR). The structure of the microreformer design based on the ZnO NR@Cu NP nanocomposite is illustrated in the Supporting Information (Scheme S1), along with photographs comparing the microchannels before and after the deposition of the ZnO NR@Cu NP nanocomposite (Supporting Information, Figure S1).

One of the most significant advantages of the core–shell nanocomposites, which are clearly distinct from traditional catalysts, is the large surface area they offer for effective surface contact between the reactants and catalysts. Figure 1a shows a cross-sectional SEM image of vertically aligned ZnO NRs grown on the inner surface of the microchannel. The size of the NRs range from 35 to 50 nm in diameter and around 5 μm in height, as determined directly from the SEM micrograph. The TEM image of a typical NR is shown in Figure 1b, indicating an uneven surface with stacking faults (marked with arrows), which is shown in greater detail in Figure 1c. Figure 1d shows a typical TEM image of ZnO@Cu hybrid nanocomposites at a copper decoration concentration of 2 mm. Close attachment of Cu NPs on the ZnO NR cores can be clearly observed. More detailed TEM images with EDX elemental mapping of copper and zinc are shown in Figure 2, which further confirms the attachment of Cu NPs on the ZnO NR cores. Furthermore, a high-resolution TEM image (Figure 1e) yielded the spacing of the {111} lattice

[*] Dr. L.-C. Chen, Dr. K.-H. Chen
Center for Condensed Matter Sciences, National Taiwan University
Taipei 106 (Taiwan)
E-mail: chenlc@ntu.edu.tw

Dr. Y.-K. Hsu, Y.-K. Lin, Dr. K.-H. Chen
Institute of Atomic and Molecular Sciences, Academia Sinica
Taipei 106 (Taiwan)
Fax: (+886) 2-2362-0200
E-mail: chenkh@pub.iams.sinica.edu.tw

Y.-G. Lin, Prof. S.-Y. Chen
Department of Materials Science and Engineering, National Chiao Tung University
Hsinchu 300 (Taiwan)

Supporting information for this article is available on the WWW under http://dx.doi.org/10.1002/anie.200902907.
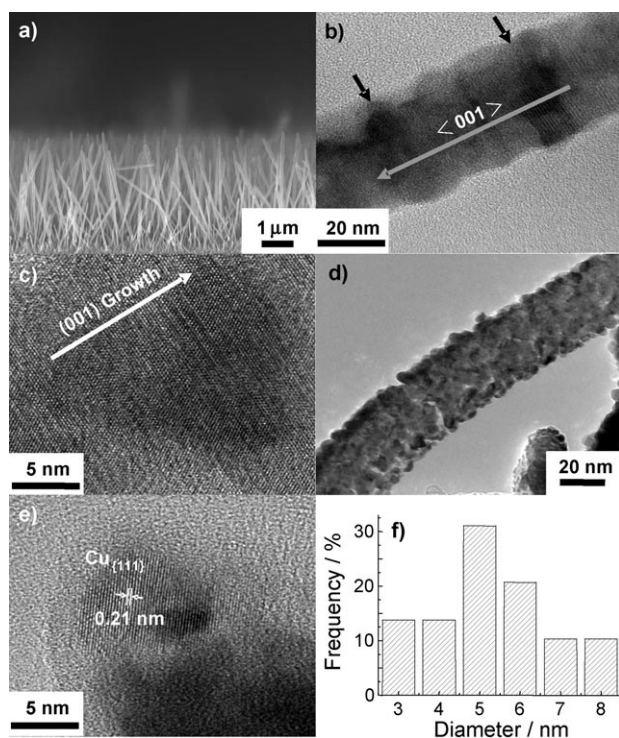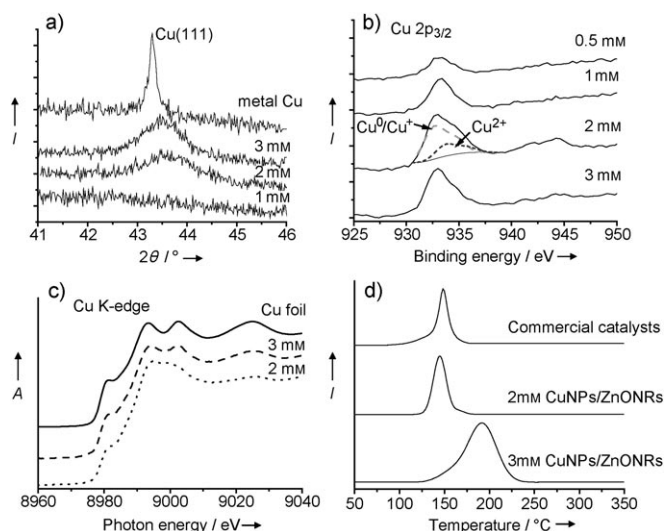
Figure 1. a) Cross-sectional SEM image of vertically well-aligned ZnO NRs. b) Typical TEM image of a single ZnO NR showing the presence of stacking faults (marked with arrows). c) HRTEM image of the ZnO NR. d) Typical TEM image of the ZnO NR@Cu NP nanocomposites. e) HRTEM image of Cu NPs on the surface of one single ZnO NR. f) The size histogram of Cu NPs analyzed from the HRTEM image.
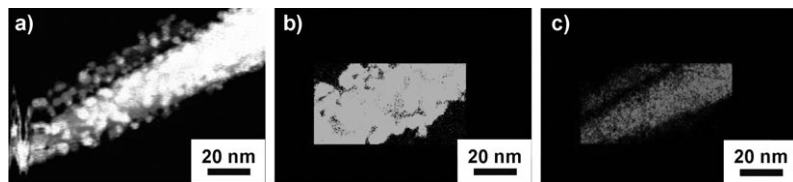
Figure 2. a) TEM image and b,c) corresponding EDX elemental mapping of b) Cu and c) Zn.

Figure 3. a) XRD patterns of Cu NPs on the surface of ZnO NRs prepared with different decoration concentrations from 1 to 3 mM. b) Cu 2p XPS core level spectra of arrayed ZnO NR@Cu NP nanocomposites prepared with different copper decoration concentrations from 0.5 to 3 mM; I = normalized intensity. c) Cu K-edge XANES spectra of arrayed ZnO NR@Cu NP nanocomposites and bulk reference sample copper foil; A = normalized absorbance. d) Comparative TPR profiles of ZnO NR@Cu NP nanocomposites and commercial catalysts (MDC-3: Sud-Chemie).

planes of the face-centered cubic copper crystal to be 0.21 nm. A histogram of the diameter of Cu NPs determined from the TEM measurement is shown in Figure 1 f, and indicates a diameter range of 3 to 8 nm, with an average of 5 nm. Moreover, a high-resolution TEM image of the Cu NP/ZnO NR heterostructures reveals that the (111) plane of the Cu NP is immobilized on the (002) plane of ZnO NR with clear evidence of the lattice-mismatched region (Supporting Information, Figure S2).

Figure 3 a shows XRD patterns of copper deposited on ZnO NRs prepared with different copper decoration concentrations of 1 to 3 mM (reference XRD patterns can be found in the Supporting Information, Figure S3). No obvious copper peak could be detected below 1 mM decoration concentration. Figure 3 a also shows that as the decoration concentration gradually increases, the Cu(111) peak at 43.5° is more prominent. The greater full-width half maximum (FWHM) of this peak for samples prepared with 2 mM and 3 mM decoration concentrations compared to that of metallic copper indicates a smaller copper particle size in the nanocomposite samples. Furthermore, the FWHM increases as the decoration concentration decreases, indicating formation of finer particles at lower decoration concentration, which is also confirmed in the results of larger copper surface area and higher dispersion determined by the N₂O decomposition method (Supporting Information, Table S1). Furthermore, in Figure 3 a, a shift in the position of this peak to higher 2θ values compared to the peak for metallic copper is also observed with decreasing decoration concentration. This effect can be attributed to the existence of defects at the interface between Cu NPs and ZnO NRs, or partial dissolution of copper into the ZnO lattice. The defects, either microstrain or structural disorder, can originate at the interface owing to lattice mismatch between copper and zinc oxide, but can be quickly overwhelmed by the strong metallic Cu(111) peak from larger particles deposited at higher decoration concentrations (Figure 3 a).

A detailed inspection of the electronic states of the surface metal species was carried out by XPS analysis. Figure 3 b depicts the Cu 2p core-level XPS of NR–Cu composite nanostructures prepared at different decoration concentrations. To differentiate between the oxidation states of copper, the main peak of the Cu 2p₃/₂ core-level spectra was fitted with two components at 932.8 and 933.7 eV corre-

sponding to Cu^0/Cu^+ and Cu^{2+} species, respectively.[18] A large fraction of copper is present as Cu^0/Cu^+ after deposition in the nanocomposite samples. Additionally, an absence of any shake-up satellite features in the spectra at binding energies above 940 eV further indicates a lower copper oxidation state.[19] When the decoration concentration was decreased, the position of the copper main peak shifted slightly toward higher binding energy, which is strongly related to the modification of the electron density on smaller copper species at lower decoration concentrations.[18] Moreover, it appears that the fraction of atomic copper on the surface, as estimated from the ratio of $Cu/(Cu+Zn+O)$ peaks tends to increase with increasing decoration concentration. In contrast, the fraction of atomic copper on the surface is lower than 8 atom % when the decoration concentration is decreased to 1 mM, which is consistent with the XRD results in Figure 3a. Meanwhile, a similar trend can be obtained for the surface ratios of Cu/Zn and ZnO/Cu by XPS measurements (Supporting Information, Table S1). However, it is rather unfortunate that the Cu^0 state cannot be distinguished from the Cu^+ state by XPS analysis owing to spectral overlap. X-ray absorption spectroscopy (XAS) measurements were therefore used to resolve this issue. X-ray absorption near-edge structure (XANES) spectra are associated with the excitation of a core electron to bound and quasi-bound states. To determine the valence of copper in the arrayed ZnO NR@-Cu NP nanocomposites, the Cu K-edge XANES spectra were compared with those of copper foil (Figure 3c). The XANES spectra of arrayed nanocomposites exhibit the edge absorption at 8979 eV together with a well-resolved doublet in the post-edge region. This result is in good agreement with that of copper foil, thus indicating a predominant presence of metallic copper in these nanocomposites. A more detailed understanding may be gained from the derivative of the XANES spectra (Supporting Information, Figure S5). The intensity of the edge absorption for arrayed nanocomposites is relatively low compared to that of copper foil, which could be related to the smaller (nano-sized) dimensions of the copper particles.[20] It may also be noted that the nanocomposite samples display lower intensity as well as a shift towards higher energy of the peak at ca. 8990 eV, together with the shoulder around 8984 eV, as compared to the derivative of copper foil. These features suggest some changes in the chemical environment around the copper species in these nanocomposites. The reason may be attributed to a further distortion of the copper lattice owing to the presence of microstrain at the interface between Cu NPs and ZnO NRs. Thus, the XAS results seem to agree well with the XRD results.

To investigate the reducibility of NR@Cu NP nanocomposites prepared at different decoration concentrations, TPR measurements were carried out in the temperature range of 140 to 300 °C (Figure 3d). It is known that the reduction of bulk CuO is indicated by a single reduction peak at a considerably higher temperature of 320 °C.[21] Clearly, the Cu NP-immobilized ZnO NR nanoarchitectures with 2 mM decoration concentration exhibits a significant shift in the position of the reduction peak to lower temperature in addition to the reduction in FWHM of the main peak as

compared to that with 3 mM decoration concentration, indicating superior redox properties of the nanocomposites. The advantage of the NR@Cu NP catalysts can be emphasized by the lower reduction temperature than the commercial catalysts (Cu-ZnO-Al$_2$O$_3$; MDC-3: Süd-Chemie) as shown in the same figure. The reason can be attributed to the enhanced dispersion of fine Cu NPs and strong metal–support interaction (SMSI) effects under NR@NP nanosystems, which facilitates the reduction of the supported copper species. However, at decoration concentrations of higher than 2 mM, the increase in the size of copper particles plays a predominant role in the structural change of ZnO@Cu nanocomposites, which also weakens the interaction between copper and zinc oxide and consequently undermines the catalytic activity.

The methanol conversion and hydrogen production rates for the arrayed ZnO@Cu nanocomposites and the commercial catalysts are shown in Figure 4a and b, respectively. Each
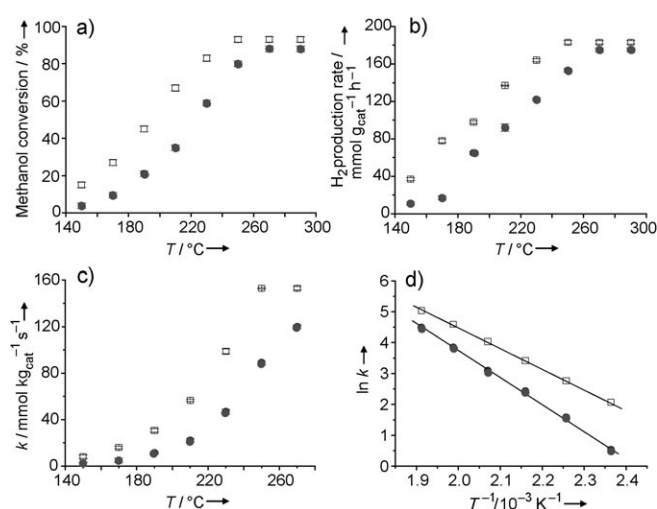
Figure 4. Comparison of arrayed Cu NP/ZnO NR nanocomposites, synthesized at 2 mM Cu(NO$_3$)$_2$ with H$_2$O/O$_2$/MeOH = 1:0.125:1, W/F = 21 kg$_{cat}$ s mol^{-1}$_{methanol}$ (□), and commercial catalysts (●), on: a) methanol reforming reaction profiles, b) hydrogen production rate as a function of reaction temperature, c) kinetic constants as a function of reaction temperature, and d) Arrhenius plots for the methanol reforming reaction.

data point represents a twelve-hour experimental run, with very little deviation observed with repeated runs, which is indicated by the small error bars in the figures. The methanol conversion rate over the arrayed ZnO@Cu nanocomposites is as high as 93%, with a hydrogen production rate of 183 mmol g$_{cat}$$^{-1}$ h^{-1} at 250 °C. Both these rates are significantly higher than those obtained with the commercial catalysts. Small amounts of carbon monoxide were detected by a CO detector in the outlet gas stream. Surprisingly, a CO concentration of only 170–210 ppm was detected during these experimental runs at 250 °C, which is much lower than circa 1000 ppm formed by the commercial catalysts. The present results thus provide a promising alternative to commercial catalysts for the catalytic generation of high-purity hydrogen without necessitating additional processes to remove CO

down-stream. For a better comparison of the catalytic activities of NR@NP nanoarchitectures and commercial catalysts, kinetic parameters were evaluated from the conversion data.[22] The kinetic constant at a given temperature can be calculated from Equation (1):

$$\kappa = 1/\tau [\varepsilon x + (1+\varepsilon)\ln(1-x)] \qquad (1)$$

where κ, τ, x, and ε are the kinetic constant, contact time, fractional conversion, and fractional expansion of the system, respectively. As shown in Figure 4c, the kinetic constant data manifest higher activity of the nanostructured NR@NP arrays than the commercial catalysts. This can be attributed to the greater external surface area, the existence of SMSI effect, the presence of microstrain at the interface, and the modification of electronic structures in the nanocomposites. These effects are consistent with the TEM, XRD, XPS, XANES, and TPR data. Based on the reaction temperature dependence of the kinetic constant, the apparent activation energy was calculated from the slope of the Arrhenius plot (Figure 4d). It is evident that the reaction activation energy for the nanostructured NR@NP arrays is noticeably lower (about 27.5 kJ mol^{-1}) than a value of 36.8 kJ mol^{-1} of the commercial catalyst, indicating that methanol reforming reaction would proceed significantly faster on these nanostructured catalysts than on the commercial catalysts. Finally, the advantage of the nanostructured NR@NP arrays catalyst is further exemplified by the higher stability (11.5% reduction after 36 h operation) in the methanol reforming reaction, which is significantly superior to the 33.8% reduction for the commercial catalysts (Figure 5).

In summary, we have successfully demonstrated an easy-to-fabricate route to prepare arrayed ZnO NR@Cu NP heterostructures on the inner surface of microchannels by direct in-situ synthesis for microreformer applications. The superb catalytic performance and stability of the Cu NP-decorated ZnO NR nanostructures can be attributed to the larger surface area and enhanced dispersion of fine Cu NPs, formation of microstrain, the modification of electronic structure of copper species, and the existence of a strong metal–support interaction effect. These results present new opportunities in the development of highly active and selective NR@NP nanoarchitectures for a wide range of different catalytic reaction systems.
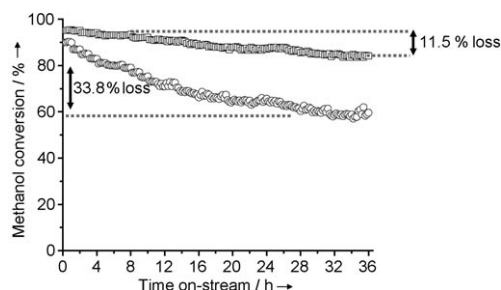
Figure 5. Stability tests for the methanol reforming reaction over arrayed Cu NP/ZnO NR nanocomposites at 2 mM (□) and commercial catalysts (○). Reaction conditions: H$_2$O/O$_2$/MeOH = 1:0.125:1, T = 250 °C, W/F = 21 kg$_{cat}$ s mol^{-1}$_{methanol}$.

Experimental Section

ZnO array preparation: A thin film of ZnO was first deposited on the inner surface of microchannels prior to the NR growth step by the solution method, which acted as a seed layer. This was followed by growth of aligned ZnO NRs on the pre-coated substrates by the chemical bath deposition (CBD) method. CBD growth was performed using equimolecular mixtures of zinc nitrate hexahydrate (99.5%, Aldrich) and hexamethylenetetramine (99%, Aldrich) as source precursors and a reaction temperature of 90 °C for 7 h. Other details of the NR array growth process were same as those described in the procedure proposed by Vayssieres.[23] A simplified attachment route, namely the direct impregnation method, was used in this study, which involved impregnation of the ZnO NR with copper nitrate trihydrate as precursor (99.5%, Aldrich), which was subsequently reduced by boiling under reflux to give to Cu/Cu$^+$ colloids. The synthesis of size-selected Cu NPs immobilized on ZnO NRs was carried out in ethylene glycol (EG) solutions as reducing agent that contained 0.5 M NaOH, with pH values between 9 and 11.[24] The decoration concentrations were controlled between 0.5 and 3 mM. The solutions were stirred for 30 min at room temperature, subsequently heated under reflux to 190 °C for 2 h, and then cooled in air. Dark brown solutions containing Cu NPs were formed in this manner and referred to as colloidal solutions in this work.

Material characterization: XRD analyses were performed on a Bruker D8 Advance diffractometer with Cu (40 kV, 40 mA) radiation. SEM measurements were made on a JEOL 6700 filed-emission SEM. XPS spectra were obtained using a Microlab 350 system. To obtain TEM images, the NR products on the microreactor were scratched and dispersed on a carbon-coated copper grid, and analyzed using a JEOL JEM-2100 TEM system. XAS analyses were performed on a beamline BL17C1 at the National Synchrotron Radiation Research Center (NSRRC), Taiwan. TPR and N$_2$O titrations were carried out with a Micromeritics AutoChem II 2920 instrument. The catalytic performance tests were conducted using an integrated microchannel reactor under atmospheric pressure. The aluminum alloy (6061) chip of the microreactor was made by ourselves through a laser machining method. Ten microchannels per aluminum alloy chip were separated by 800 μm fins. The width, depth, and length of the microchannels were 500 μm, 200 μm, and 4.3 cm, respectively. For the calculation of the catalyst weight for the steam reforming reactions, we measured the total weight including Cu NP/ZnO NR nanocomposites without the ZnO seed layer with a precision electronic balance (±0.1 mg; Sartorius). The commercial CuO-ZnO-Al$_2$O$_3$ catalysts (Sud-Chemie; MDC-3) were used as reference sample and were deposited on the inner surface of microchannels using the wash-coating method.[16] After reduction of catalysts in a H$_2$/N$_2$ (5/95) at a flow rate of 50 mL min^{-1} at 200 °C for 1 h, premixed water, oxygen, and methanol with a H$_2$O/O$_2$/MeOH molar ratio of 1:0.125:1 were fed into the preheater maintained at 200 °C by means of microfeeder. The feed and product gas streams were analyzed online with a thermal conductivity detector gas chromatograph (TCD-GC; China Chromatography Co., Ltd) and CO detector (Gastech CO., Ltd.; GTF200).

[1] M. Z. Jacobson, W. G. Colella, D. M. Golden, *Science* **2005**, *308*, 1901.
[2] R. R. Davda, J. A. Dumesic, *Angew. Chem.* **2003**, *115*, 4202; *Angew. Chem. Int. Ed.* **2003**, *42*, 4068.

[3] G. A. Deluga, J. R. Salge, L. D. Schmidt, X. E. Verykios, *Science* **2004**, *303*, 993.

[4] B. L. Kniep, T. Ressler, A. Rabis, F. Girgsdies, M. Baenitz, F. Steglich, R. Schlögl, *Angew. Chem.* **2004**, *116*, 114; *Angew. Chem. Int. Ed.* **2004**, *43*, 112.

[5] B. Frank, F. C. Jentoft, H. Soerijanto, J. Kröhnert, R. Schlögl, R. Schomäcker, *J. Catal.* **2007**, *246*, 177.

[6] Y. Choi, H. G. Stenger, *J. Power Sources* **2005**, *142*, 81.

[7] R. Becker, H. Parala, F. Hipler, O. P. Tkachenko, K. V. Klementiev, W. Grünert, H. Wilmer, O. Hinrichsen, M. Muhler, A. Birkner, C. Wöll, S. Schäfer, R. A. Fischer, *Angew. Chem.* **2004**, *116*, 2899; *Angew. Chem. Int. Ed.* **2004**, *43*, 2839.

[8] T. Ressler, B. L. Kniep, I. Kasatkin, R. Schlögl, *Angew. Chem.* **2005**, *117*, 4782; *Angew. Chem. Int. Ed.* **2005**, *44*, 4704.

[9] S. Vukojević, O. Trapp, J. D. Grunwaldt, C. Kiener, F. Schüth, *Angew. Chem.* **2005**, *117*, 8192; *Angew. Chem. Int. Ed.* **2005**, *44*, 7978.

[10] I. Kasatkin, P. Kurr, B. Kniep, A. Trunscke, R. Schlögl, *Angew. Chem.* **2007**, *119*, 7465; *Angew. Chem. Int. Ed.* **2007**, *46*, 7324.

[11] L. C. Wang, Y. M. Liu, M. Chen, Y. Cao, H. Y. He, G. S. Wu, W. L. Dai, K. N. Fan, *J. Catal.* **2007**, *246*, 193.

[12] E. N. Muhamad, R. Irmawati, Y. H. Taufiq-Yap, A. H. Abdullah, B. L. Kniep, F. Girgsdies, T. Ressler, *Catal. Today* **2008**, *131*, 118.

[13] O. J. Kwon, S. M. Hwang, J. H. Chae, M. S. Kang, J. J. Kim, *J. Power Sources* **2007**, *165*, 342.

[14] J. S. Suh, M. T. Lee, R. Greif, C. P. Grigoropoulos, *J. Power Sources* **2007**, *173*, 458.

[15] A. Stefanescu, A. C. van Veen, C. Mirodatos, J. C. Beziat, E. Duval-Brunel, *Catal. Today* **2007**, *125*, 16.

[16] Y. Kawamura, N. Ogura, T. Yamamoto, A. Igarashi, *Chem. Eng. Sci.* **2006**, *61*, 1092.

[17] A. Kundu, J. E. Ahn, S. S. Park, Y. G. Shul, H. S. Han, *Chem. Eng. J.* **2008**, *135*, 113.

[18] C. D. Wagner, W. M. Riggs, L. E. Davis, J. F. Mouler, *Handbook of X-Ray Photoeletron Spectroscopy*, Perkin–Elmer Corporation, MN, **1979**.

[19] S. Velu, K. Suzuki, C. S. Gopinath, *J. Phys. Chem. B* **2002**, *106*, 12737.

[20] D. Grandjean, H. L. Castricum, J. C. Heuvel, B. M. Weckhuysen, *J. Phys. Chem. B* **2006**, *110*, 16892.

[21] C. Z. Yao, L. C. Wang, Y. M. Liu, G. S. Wu, Y. Cao, W. L. Dai, H. Y. He, K. N. Fan, *Appl. Catal. A* **2006**, *297*, 151.

[22] M. Turco, G. Bagnasco, C. Cammarano, P. Senese, U. Costantino, M. Sisani, *Appl. Catal. B* **2007**, *77*, 46.

[23] L. Vayssieres, *Adv. Mater.* **2003**, *15*, 464.

[24] C. Bock, C. Paquet, M. Couillard, G. A. Botton, B. R. MacDougall, *J. Am. Chem. Soc.* **2004**, *126*, 8028.